Bull. Mater. Sci., Vol. 31, No. 3, June 2008, pp. 433–439. © Indian Academy of Sciences.

Studies on crystallization behaviour and mechanical properties of Al–Ni–La metallic glasses

K L SAHOO*, RINA SAHU, M GHOSH and S CHATTERJEE[†]

Metal Extraction and Forming Division, National Metallurgical Laboratory, Jamshedpur 831 007, India
[†]Department of Metallurgical and Materials Engineering, Bengal Engineering and Science University, Howrah 711 103, India

Abstract. **Alloy ingots with nominal composition, $Al_{92-x}Ni_8La_x$ (x = 4 to 6) and $Al_{94-x}Ni_6La_x$ (x = 6, 7), were prepared by induction melting in a purified Ar atmosphere. Each ingot was inductively re-melted and rapidly solidified ribbons were obtained by ejecting the melt onto a rotating copper wheel in an argon atmosphere. The crystallization behaviour of melt-spun amorphous ribbon was investigated by means of differential scanning calorimetry (DSC), X-ray diffractometry and transmission electron microscopy. DSC showed that $Al_{86}Ni_8La_6$ alloy undergoes a three-stage and rest of the alloys undergo a two-stage crystallization process upon heating. The phases responsible for each stage of crystallization were identified. During the first crystallization stage *fcc*-Al precipitates for low La-containing alloys and for higher La-containing alloys a *bcc* metastable phase precipitates. The second crystallization stage is due to formation of intermetallic compounds along with *fcc*-Al. Microhardness of all the ribbons was examined at different temperatures and correlated with structural evolutions. Precipitation strengthening of nano-size *fcc*-Al is responsible for maximum hardness in these annealed alloys.**

Keywords. **Metallic glass; Al–Ni–La alloys; XRD; crystallization.**

1. Introduction

Increasing demand for high performance engineering components continuously drives the development of new advanced materials. Amorphous and nanocrystalline alloys are examples of such materials. Al-based amorphous alloys have attracted considerable attention in the last two decades due to the occurrence of a primary crystallization reaction that yields a microstructure consisting of uniformly dispersed Al-nanocrystals embedded in an amorphous matrix. These alloys possess high specific strength coupled with good ductility, high hardness, and good wear and corrosion resistance. However, these favourable properties fall off if the alloys crystallize to a grain size that exceeds the nanometre range. Growth of these nano-crystals could be retarded by choosing alloy composition, which lead to higher activation energy of crystallization and/or introduce a thermal barrier for crystallization (Inoue 1998).

Among the Al-based amorphous alloys, Al–Ni–RE (RE = Y, or rare-earth elements) with Al content between 80 and 90 at.% have attracted considerable attention due to their wide glass formation ranges. By partial crystallization, one can tailor alloy properties that are an important prerequisite for its use as an advanced engineering material. Gangopadhyay and Kelton (2000) investigated the crystallization process in Al–Ni–RE amorphous alloys and found that crystallization products depend on the radius of the rare-earth atoms. They showed that alloys containing smaller radius RE elements produce *fcc*-Al while larger radius RE elements produce metastable intermetallic phases as primary crystallization product. In contrast, Gogebakan *et al* (1997) reported that the first crystallization products in $Al_{85}Ni_4Y_{11}$ are *fcc*-Al, Al_3Y and some unidentified metastable intermetallic phases. The formation of a *fcc*-Al phase after the first crystallization stage was reported by Ye and Lu (1999) in $Al_{89}Ni_5La_6$ and Sahoo *et al* (2004) in $Al_{90}Ni_6La_4$, whereas Zhuang *et al* (2001) reported eutectic crystallization of *fcc*-Al and metastable *bcc*-$(AlNi)_{11}La_3$-like phase in $Al_{89}Ni_5La_6$ alloy. No systematic report is available on the nature of crystallization product in Al–Ni–La alloys.

In this present paper, the thermal stability, crystallization pathways and evolution of microhardness of Al–Ni–La amorphous alloys containing 6 and 8 at.% Ni and varying amounts of La are investigated. Microstructural evolution of alloys with temperature is correlated with the microhardness.

2. Experimental

Ingots with compositions, $Al_{88}Ni_8La_4$ (A84), $Al_{87}Ni_8La_5$ (A85), $Al_{86}Ni_8La_6$ (A86), $Al_{88}Ni_6La_6$ (A66) and $Al_{87}Ni_6La_7$ (A67), were prepared by alloying pure components (puri-

*Author for correspondence (klsah@nmlindia.org)

ties were 5N Al; 4N Ni; 3N La) by induction melting under a purified argon atmosphere (purity: 99·999%). The ingot was inductively re-melted (temperature ranges from 1280–1300 K) and melt-spun ribbons were prepared by ejecting the melt onto a rotating copper wheel (rotational speed: 40 m/s) in He atmosphere.

The amorphous nature of the as-prepared ribbons was proved by XRD (Siemens, 40 kV, 40 mA, CuK_{α}, scan rate 0.15° min^{-1}) and TEM (Philips CM200). The crystallization behaviour of the ribbons was studied by DSC (DSC-7, Perkin-Elmer) under a high purity argon atmosphere. The DSC was calibrated by using pure In and Zn standards, giving an accuracy of ± 0·3 K for temperature and ± 0·02 mW for the heat flow measurements. The isochronal DSC study was conducted at different heating rates ranging from 10–40 K/min. For scanning at a constant heating rate, a second scan was used as a base line. The TEM samples were prepared by electrochemical dissolution method using a solution of 25% nitric acid and 75% methanol at 243 K and 12 V. The evolution of hardness with temperature was investigated using a Paar Physica microhardness tester (MHT-10, Anton Paar) under a 0·2 N load.

3. Results

3.1 *XRD studies*

The ribbons prepared by melt spinning are 30 ± 5 μm in thickness, 1–2 mm wide and several meters long. All the ribbons show good bend ductility. XRD patterns revealed that all the melt-spun ribbons were fully amorphous on the substrate side (not shown) as well as on the air-cooled side (figure 1). All the as-quenched samples showed a distinct broad and a small diffuse maximum centred around 37° and 66°, respectively which are characteristics of a glassy phase. In addition to these diffuse maxima, a small pre-peak at 2θ = 15–24° exists in all the ribbons.

3.2 *DSC studies*

The ribbons are heated continuously in DSC at heating rates varying from 10–40 K/min. Figure 2 represents the DSC curves of the amorphous alloys heated at a rate of 40 K/min. The influence of alloy composition on the heat effects and their positions is revealed in figure 2. Two or three exothermic peaks corresponding to the crystallization of the phases are observed in different temperature ranges. The peak temperature for crystallization and the activation energy for the formation of phases are shown in table 1. The first T_p increases whereas the second T_p decreases with higher La content. The onset and peak temperatures of the crystallizations are shifted towards higher temperatures when the heating rate is raised except for the A86 alloy where the second crystallization temperature decreases with increasing heating rate. This is due to appearance of the third peak. The activation energy (E_a) of the crystallization stages are determined by Kissinger (1957) analysis

$$\ln\left(\frac{T_p^2}{\beta}\right) = \left(\frac{E_a}{RT_p}\right) + A, \tag{1}$$

where β is the heating rate, T_p the peak temperature in Kelvin, R the gas constant and A a constant. The values of activation energies for all crystallization stages are shown in table 1.

In order to identify the phases responsible for the crystallization stages in the DSC curve, different samples

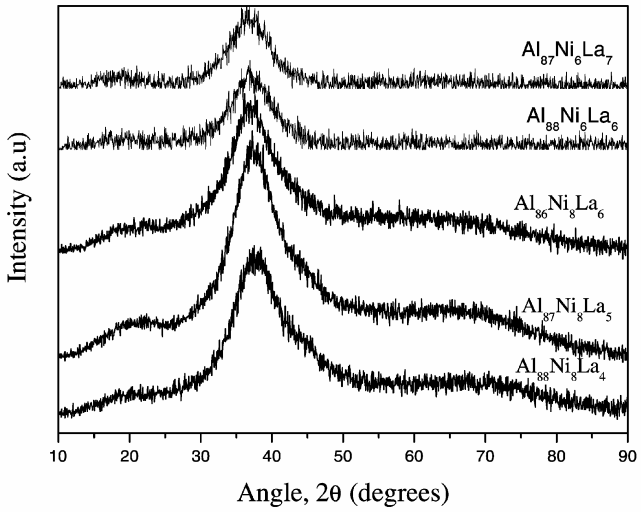

Figure 1. XRD patterns of as-melt-spun Al–Ni–La amorphous ribbons on the air-cooled side.

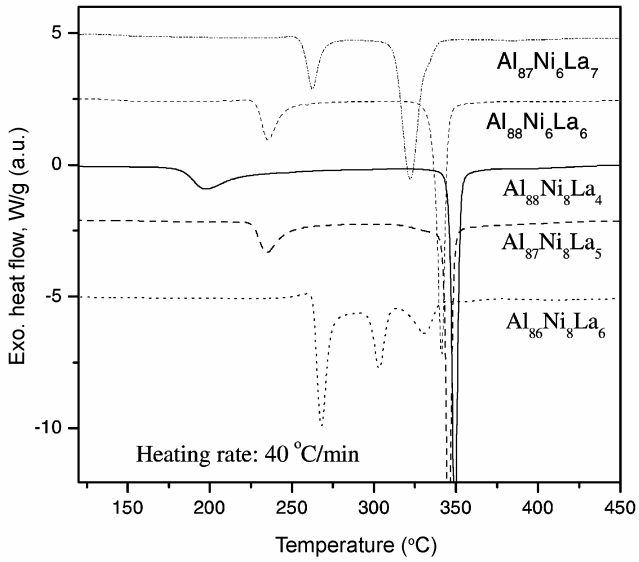

Figure 2. Continuous heating of DSC curves of amorphous Al–Ni–La alloys at a heating rate of 40 K/min.

Table 1. Peak temperatures at different heating rates and activation energy for the different stages of crystallization.

Alloy system	Crystallization stages	Peak temperature (°C) at different heating rates				
		10 K/min	20 K/min	30 K/min	40 K/min	E_a (kJ/mol)
A66	1st peak	224	230	233	236	257 ± 7
	2nd peak	321	331	337	341	194 ± 1
A67	1st peak	246	256	262	267	148 ± 6
	2nd peak	309	317	321	323	355 ± 12
A84	1st peak	186	192	195	197	207 ± 12
	2nd peak	329	339	345	349	200 ± 1
A85	1st peak	224	229	232	235	258 ± 7
	2nd peak	325	335	341	345	201 ± 1
A86	1st peak	255	261	265	268	253 ± 16
	2nd peak	306	305	304	303	–
	3rd peak	–	317	326	331	164 ± 8

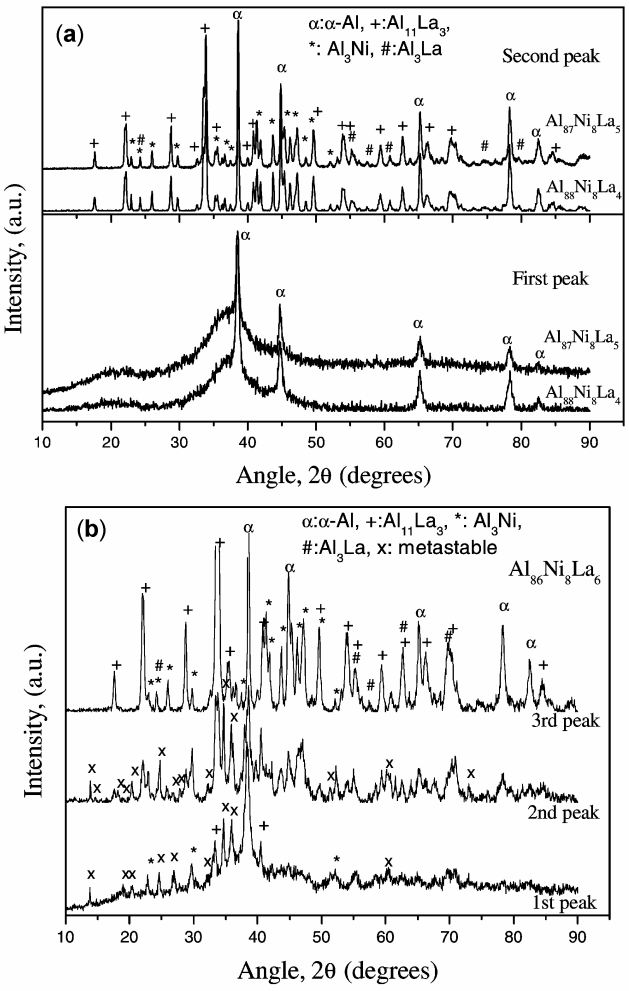

Figure 3. XRD patterns of amorphous Al–Ni–La alloys heated up to the end of crystallization temperatures: (**a**) $Al_{88}Ni_8La_4$ and $Al_{87}Ni_8La_5$ and (**b**) $Al_{86}Ni_8La_6$.

were heated in the DSC up to the end of their peaks. All the samples were heated up to the respective crystallization stages at a rate of 40 K/min. The XRD patterns of all the corresponding samples are shown in figures 3 and 4. Figure 3(a) shows that the first crystallization stage in A84 and A85 alloys is due to the formation of *fcc*-Al. The second crystallization stage in these alloys is due to formation of $Al_{11}La_3$, Al_3La and Al_3Ni (figure 3a). In A86 alloy, the first crystallization stage is due to the formation of mainly an unknown metastable phase, *fcc*-Al and a small amount of $Al_{11}La_3$ and Al_3Ni (figure 3b). The second crystallization stage is due to formation of $Al_{11}La_3$, Al_3La and Al_3Ni from the remaining amorphous matrix and their growth. The third crystallization stage is due to transformation of metastable phases into stable phases probably of Al, $Al_{11}La_3$ and Al_3Ni phases. In case of A66 alloy, the first crystallization stage is due to formation of both *fcc*-Al and a metastable phase (figure 4a). The Bragg angles of the latter phase do not match either with *fcc*-Al or with any known binary or ternary compound of Al, Ni and La. In A67 alloy, formation of *fcc*-Al was not detected in the first crystallization stage. Instead, only the metastable phase was observed. Analysing the patterns using the programme 'powder cell' and Rietveld refinement (Rietveld 1969), best agreement with respect to position and intensity of the reflections is achieved for a body-centred cubic (*bcc*) phase with a lattice parameter of 0·663 nm. Since, the intensity of the diffraction peaks corresponding to the metastable *bcc* phase is high in comparison to the remaining halo or the *fcc*-Al phase, it is reasonable to presume that the phase contains a significant amount of an element with a higher atomic number, i.e. La. The second crystallization stage in A66 and A67 alloys is due to formation of Al, $Al_{11}La_3$ and Al_3Ni phases (figure 4b).

3.3 *Isochronal microhardness*

Figure 5 shows the variation of microhardness with temperature. Different ribbons were annealed for 10 min at di-

fferent temperatures starting from room temperature to 480°C. The hardness values shown in figure 5 are the average of about 10 measurements on each sample and the corresponding errors are shown for each data point. The highest hardness values were detected at around 290°C for A66 and A85 alloys and at around 270°C for A67 and A86 alloys (the hardness graph for A67, A66 and A84 alloys are not shown here).

3.4 *TEM studies*

Figure 6 shows the representative TEM selected area diffraction (SAD) pattern of as melt-spun A85 alloy. In accordance with the XRD results no appreciable contrast revealing crystals is seen. The representative TEM image obtained from A85 ribbon, annealed at 290°C for 10 min, is shown in figure 7a. In figure 7a, the SAD pattern shows a broad ring of intensity stemming from the amorphous matrix and rings of diffraction peaks caused by precipitation in amorphous matrix. The dark-field (DF) image was obtained by placing the aperture on the part of the diffuse ring as well as the {111} and {200} diffraction rings. Therefore, Al precipitates are visible in the image either as bright (in contrast) or dark (out of contrast) patches. From the diffraction rings lattice constant was found to be 0·405 nm. The size of precipitates ranges from a few nanometres to about 40 nm for large conglomerates. Figure 7b shows the TEM dark field image from A85 ribbon annealed at 300°C for 10 min. The inset depicts the corresponding SAD pattern, which reveals a large set of diffraction rings but no indication for an amorphous phase. The size of the precipitates ranges between about 20 and 80 nm.

4. Discussion

The materials obtained by melt spinning appear to be amorphous in XRD studies. In spite of this observation,

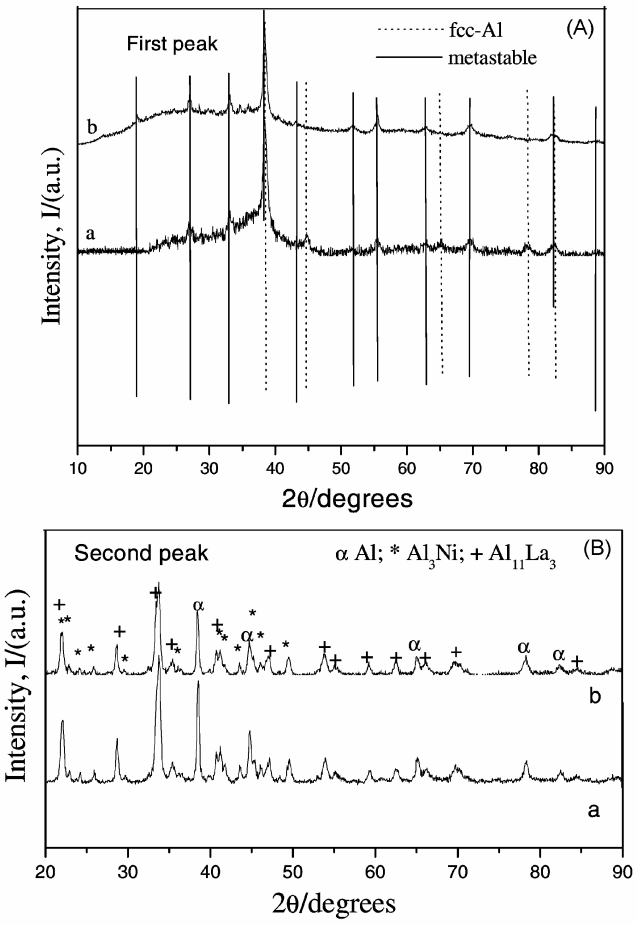

Figure 4. XRD patterns of Al–Ni–La alloys heated up to the end of crystallization temperatures (**A**) $Al_{88}Ni_6La_6$ and (**B**) $Al_{87}Ni_6La_7$.

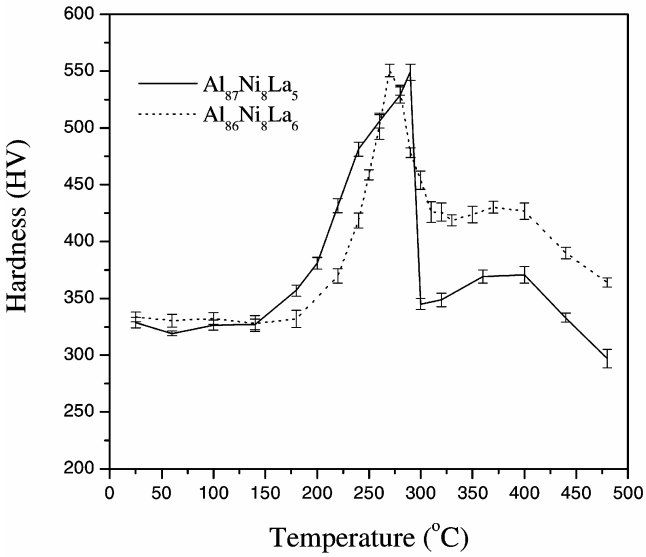

Figure 5. Isochronal microhardness evolution of different $Al_{92-x}Ni_8La_x$ ribbons. The samples were annealed for 10 min at each measurement temperature.

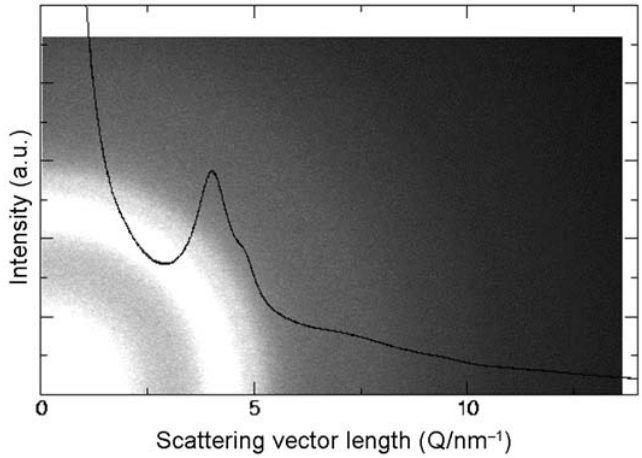

Figure 6. Representative TEM SAD pattern of a as-melt-spun A85 specimen.

DSC does not show clear glass transition temperature (T_g), except for the A86 alloy (figure 2). The reason may be that T_g is hidden underneath the first crystallization stage. Accurate measurement of T_g could be done by using temperature modulated DSC (TMDSC) which will separate the reversible heat flow and non-reversible heat flow from the total heat flow (Lu *et al* 2004). Alloy A86 showed clear glass transition temperature at all heating rates due to higher first crystallization peak temperature, T_{P1} (268°C), than the T_g (248°C). The enthalpy associated with the glass transition is around 1·9 J/g when the sample is heated at 40 K/min. All the alloys showed (figure 1) a small pre-peak at $2\theta = 15$–$24°$. The observation of a pre-peak is an evidence of either for chemical short-range order in the sense of compound-forming behaviour (Steeb and Lamparter 1984) or for the presence of clusters constituted of unlike atoms (Hoyer and Jodicke 1995). Schmidt *et al* (2001) reported that the development of a pre-peak monitor changes in the short-range order between the atoms. We recently also observed the presence of small clusters or at least concentration fluctuations on a nanometre scale in as melt spun alloys by small angle neutron scattering (Sahoo *et al* 2005). Thus, the compound-forming tendency cannot be excluded in the present as melt spun alloys.

The peak of the first crystallization stage is distinctly asymmetric with a tail towards higher temperature (figure 2). The first crystallization peak temperature increases and the second crystallization peak temperature decreases with increasing La content for a fixed Ni composition. This fits into the general tendency that higher Al contents lower thermal stability of Al–Ni–La alloys. The observed changes of the first and second crystallization temperatures are in good agreement with the data for other Al–Ni–La alloys in the literature (Inoue 1998; Gangopadhyay and Kelton 2000). XRD analyses of specimens annealed to about the end of crystallization events as observed by DSC (figure 2) revealed two-stage crystallization pathways for all the ribbons except A86 that shows three-stage crystallization pathways. The *fcc*-Al formed during the first stage of crystallization in alloys A84 and A85 yields a lattice constant of 405·4 pm, which is nearly same as of pure Al (404·9 pm). The representative crystallization peak temperatures in a ternary diagram are shown in figure 8. The grey shaded hexagons show the temperatures from our measurements whereas the open hexagons contain values from the literature. In the hexagon, the lower value indicates first crystallization peak temperature and the upper value indicates the second crystallization peak temperature. The dashed line approximately divides two regions of different crystallization behaviour. The evolution of first peak temperature shows a change in slope for all heating rates at La concentration of ≥ 6 at.%. The overall tendency is that the first peak temperature increases while the second peak temperature is reduced with increasing La and Ni contents (including the binary Al–La alloys). It can be seen that there is a

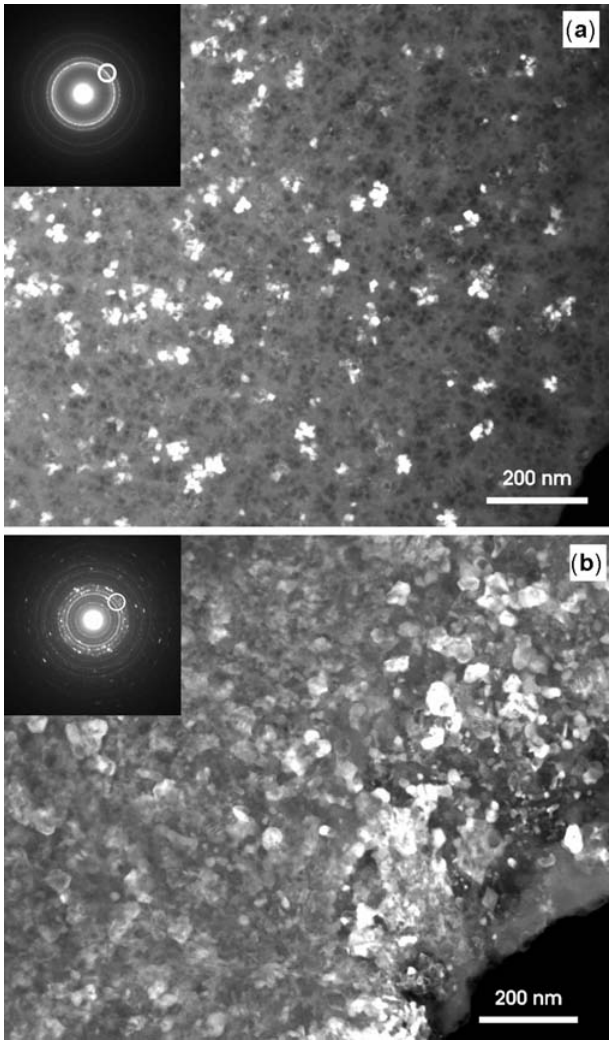

Figure 7. TEM dark field image and inset SAD of A85 alloys annealed for ten minutes: (**a**) 290°C and (**b**) 300°C. Circle on SAD patterns show the position from where dark field was taken.

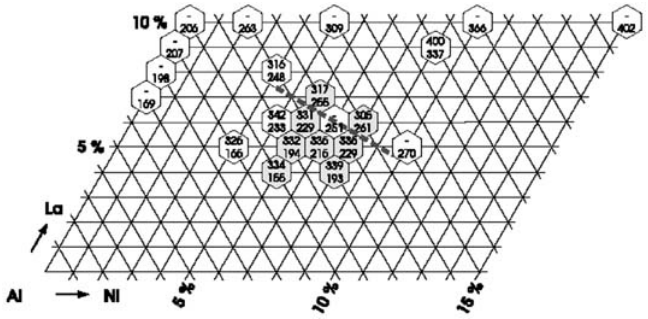

Figure 8. Representation of crystallization peak temperatures in a ternary diagram of Al–La binary and Al–Ni–La ternary alloys.

jump in crystallization temperature whenever the line drawn in figure 8 is crossed.

The as melt-spun ribbons show higher hardness with increasing La concentration (figure 5) indicating different initial microstructures of the ribbons. The different manner of evolution of heat flow with time at a constant temperature also indicated different structural states of the ribbons. Hardness does not change much from room temperature to about 150°C. This is due to the fact that the microstructure does not change appreciably as these glasses are thermally stable at lower temperatures. Thereafter, a sharp increase of hardness with increasing temperature is observed which is caused by crystallization of *fcc*-Al (for low La content) or metastable phase (for high La content) leading to precipitation strengthening of the material. At the point where highest hardness is observed, the matrix is still amorphous (figure 7a). The solid solubility of Ni and La in Al at the equilibrium eutectic temperature of each binary system is about 0·01 at.% (Gschneider and Calderwood 1986; Singleton *et al* 1986). Rapidly solidified Al-rich Al–Ni alloy extends the solid solubility limit of Ni in Al from 0·01 at.% to as much as 7·7 at.% (Singleton *et al* 1986). Therefore, with the crystallization and growth of Al particles from the rapidly solidified amorphous alloys, Ni and La, are rejected and the remaining amorphous matrix gets richer in solute elements leading to stable amorphous matrix. It is reported that rare earth elements diffuse much slower in Al than in Ni and Fe (Hono *et al* 1995). The diffusivity of La in these alloy systems may be lower than those of Al and Ni by orders of magnitude because of its larger atomic radius. Hence, during the growth of Al particles, the rejected La atoms are enriched at the Al/amorphous interface and the interface must reject La for further growth. This would effectively slow down the growth of Al particles. With temperature, the increase in diffusivity of the elements yields additional nucleation and a substantial increase in the initial particle growth rate. Crystallization at higher temperatures (above 290°C for A85 alloy), leading to substantial growth of Al particles (figure 7a) and to decomposition of the amorphous matrix leading to precipitation of intermetallic particles (mainly, $Al_{11}La_3$ and Al_3Ni) from the matrix (figure 7b), results in a sharp drop of hardness. The TEM DF image shows (figure 7b) that the precipitates are bigger in size compared to that for the specimen annealed at 290°C and also shows a wide range of sizes. With the progress of crystallization hardness increases again due to the increased volume fraction of crystallized intermetallic particles. Later on, the decrease of hardness with higher temperature is due to coarsening of the particles (figure not shown). Microhardness evolution with temperature in A86 alloy is different from other alloys because of the formation of different kinds of crystallites during the various stages of crystallization. The slower drop of hardness after 270°C is due to transformation of metastable phases to *fcc*-Al and intermetallic phases. In the fully crystallized state hardness increases with La content due to an increased amount of intermetallic phases in the matrix. The plastic deformation in such type of metallic glasses could be explained by studying the morphological characteristics of the indentation deformation zones. In this context, a good number of literatures are available that deal with the mechanical behaviour, mainly plastic deformation, in amorphous and partially crystallized bulk metallic glasses (Basu *et al* 2003; Ramamurty *et al* 2005; Schuh *et al* 2007).

5. Conclusions

The results showed that the variation of La content in Al–Ni–La alloys has significant influence on the crystallization pathways from amorphous to stable crystalline phases and on the evolution of microhardness with temperature.

DSC and XRD analyses revealed two-stage crystallization pathways for all the ribbons except A86 that shows three-stage crystallization pathways.

The two stages of crystallization in $Al_{88}Ni_8La_4$ (A84) and $Al_{87}Ni_8La_5$ (A85) alloy correspond to the formation of *fcc*-Al and $Al_{11}La_3$, Al_3Ni, Al_3La, respectively. We report the three-stage crystallization in $Al_{86}Ni_8La_6$ (A86) alloy, which corresponds to formation of metastable phase, *fcc*-Al, $Al_{11}La_3$, Al_3Ni (first stage), $Al_{11}La_3$, Al_3Ni, Al_3La (second stage) and decomposition of metastable phase to stable crystalline phases (third stage).

The first crystallization temperature increases while the second one decreases with increasing La concentration.

The higher microhardness with increasing La content indicates different structural state of initial ribbons. The hardness does not change appreciably up to the temperature of 150°C indicating the structural stability at lower temperatures. Thereafter, the sharp increase of hardness is due to nanoscale precipitation of primary crystallization product. The rapid fall of hardness in A84 and A85 alloys after 290°C and in A86 alloy after 270°C is due to decomposition of amorphous matrix and formation of intermetallic compounds.

Acknowledgement

The authors wish to thank DST (NSTI) for sponsoring the project, grant. No. SR/S5/NM-78/2002.

References

Basu J, Nagendra N, Li Y and Ramamurty U 2003 *Philos. Mag.* **83** 1747

Gangopadhyay A K and Kelton K F 2000 *Philos. Mag.* **A80** 1193

Gogebakan M, Warren P J and Cantor B 1997 *Mater. Sci. Eng.* **A226** 168

Gschneider Jr K A and Calderwood F W 1986 *Binary alloy phase diagram* (ed.) T B Massalski (Metals Park, Ohio: American Society for Metals) **Vol. 1**

Hono K, Zhang Y, Inoue A and Sakurai T 1995 *Mater. Trans. JIM* **36** 909
Hoyer W and Jodicke R 1995 *J. Non-Cryst. Solids* **192–193** 102
Inoue A 1998 *Prog. Mater. Sci.* **43** 365
Kissinger H E 1957 *Anal. Chem.* **29** 1702
Lu Z P, Liu C T and Li Y 2004 *Intermetallics* **12** 869
Ramamurty U, Jana S, Kawamura Y and Chattopadhyay K 2005 *Acta Mater.* **53** 705
Rietveld H M 1969 *J. Appl. Crystallogr.* **2** 65
Sahoo K L, Panda A K, Das S and Rao V 2004 *Mater. Letts* **58** 316
Sahoo K L, Wollgarten M, Haug J and Banhart J 2005 *Acta Mater.* **53** 3861
Schmidt U, Eisenschmidt C, Zahra C Y and Zahra A -M 2001 *J. Non-Cryst. Solids* **289** 75
Schuh C A, Hufnagel T C and Ramamurty U 2007 *Acta Mater.* **55** 4067
Singleton M F, Murray J L and Nash P 1986 *Binary alloy phase diagram* (ed.) T B Massalski (Metals Park, Ohio: American Society for Metals) **Vol. 1**
Steeb S and Lamparter P 1984 *J. Non-Cryst. Solids* **61–62** 237
Ye F and Lu K 1999 *Acta Mater.* **47** 2449
Zhuang Y X, Jiang J Z, Lin Z G, Mezouar M, Crichton W and Inoue A 2001 *Appl. Phys. Lett.* **79** 743